

# MUSE observations of the ionized gas in a galaxy group at $z = 0.45$ with 21-cm H I absorption towards PKS 1610-771

Simon Weng,<sup>1,2,3\*</sup> Elaine M. Sadler,<sup>1,2,3</sup> Caroline Foster,<sup>1,3</sup> Céline Péroux,<sup>4,5</sup>  
Elizabeth K. Mahony,<sup>2</sup> James R. Allison,<sup>3,6</sup> Vanessa A. Moss,<sup>2,1</sup> Renzhi Su,<sup>2,7</sup>  
Matthew T. Whiting<sup>2</sup> and Hyein Yoon<sup>1,3</sup>

<sup>1</sup>*Sydney Institute for Astronomy, School of Physics, University of Sydney, NSW 2006, Australia*

<sup>2</sup>*ATNF, CSIRO Astronomy and Space Science, PO Box 76, Epping, NSW 1710, Australia*

<sup>3</sup>*ARC Centre of Excellence for All Sky Astrophysics in 3 Dimensions (ASTRO 3D)*

<sup>4</sup>*European Southern Observatory, Karl-Schwarzschildstrasse 2, D-85748 Garching bei München, Germany*

<sup>5</sup>*Aix Marseille Université, CNRS, LAM (Laboratoire d'Astrophysique de Marseille) UMR 7326, F-13388 Marseille, France*

<sup>6</sup>*Sub-Dept. of Astrophysics, Department of Physics, University of Oxford, Denys Wilkinson Building, Keble Rd., Oxford, OX1 3RH, UK*

<sup>7</sup>*Shanghai Astronomical Observatory, Chinese Academy of Sciences, 80 Nandan Road, Shanghai 200030, China*

Accepted XXX. Received YYY; in original form ZZZ

## ABSTRACT

We present results from MUSE observations following up on a 21-cm H I absorption system detected with the Australian Square Kilometre Array Pathfinder radio telescope at redshift 0.4503 towards the quasar PKS 1610-771. This H I absorber has a column density  $N_{\text{H I}} = 2.7 \pm 0.1 \times 10^{20} \cdot [\text{T}_s/100\text{K}] \cdot \text{cm}^{-2}$ , making it a likely Damped Lyman- $\alpha$  (DLA) system. We identify a galaxy group with four members (A, B, X and Y) at the same redshift as the H I absorption system, with impact parameters ranging from less than 10 kpc to almost 200 kpc from the quasar sightline. Ca II and Na I absorption is also seen in the MUSE spectrum of the background QSO, with velocities coinciding with the initial H I 21-cm detection, but tracing less dense and potentially warmer gas. This metal-line component aligns with the rotating ionized disc of galaxy B (impact parameter 18 kpc from the QSO) and appears to be co-rotating with the galaxy disc, although outflowing gas cannot be directly excluded. In contrast, the 21-cm H I absorber is blueshifted relative to the galaxies nearest the absorber and has the opposite sign to the velocity field of galaxy B. Since galaxies A and B are separated by only 17 kpc on the sky and 70 km s<sup>-1</sup> in velocity, it is likely that the 21-cm detection traces extragalactic clouds of gas formed from their interaction. This system represents a first case study of the cold gas detected in galaxy groups by future large 21-cm absorption surveys, such as the First Large Absorption Survey in H I.

**Key words:** intergalactic medium – galaxies: kinematics and dynamics – quasars: absorption lines – radio lines: ISM

## 1 INTRODUCTION

The reservoirs of cold gas within galaxies serve as fuel for star formation, which in turn drives the morphological and kinematic properties of galaxies. It follows that the availability of hydrogen and phenomena that affect this availability play an important role in how galaxies evolve (Péroux & Howk 2020). Placing observational constraints on the amount and distribution of gas across all redshifts will improve our understanding of galaxy evolution. Processes that

affect gas abundance such as inflows and outflows also require characterisation from observations as we pursue more complete simulations of the baryon cycle.

The amount and distribution of neutral hydrogen (H I) is well-constrained at low redshift ( $z \lesssim 0.1$ ) from H I emission-line surveys Rosenberg & Schneider (2002); Zwaan et al. (2005); Hoppmann et al. (2015); Giovanelli & Haynes (2015); Jones et al. (2018). Beyond this redshift, 21-cm emission is too faint for detection without stacking techniques (e.g. Kanekar et al. 2016; Rhee et al. 2018; Chowdhury et al. 2020) as the transition rate is highly forbidden. While H I emission line stacking can extend the search for neu-

\* E-mail: swen2649@uni.sydney.edu.au (KTS)

tral gas beyond the local Universe, the amount and distribution of gas still remains uncertain at intermediate redshifts ( $0.2 \leq z \leq 1.7$ ). At  $z \gtrsim 1.7$ , optical observations of Ly- $\alpha$  1215 Å absorption in background quasar spectra constrain the cosmic density of hydrogen (e.g. [Noterdaeme et al. 2012](#)). These damped Lyman- $\alpha$  absorbers (DLAs) trace column densities above  $2 \times 10^{20}$  atoms cm $^{-2}$  and account for  $\sim 80\%$  of the cosmic neutral gas density ([Péroutx et al. 2003; Noterdaeme et al. 2009, 2012; Zafar et al. 2013; Berg et al. 2019](#)). This technique has been extended to lower redshifts by first selecting candidate systems with strong Mg II absorption and then following up with Hubble Space Telescope (HST) Ultraviolet spectroscopy to search for Ly- $\alpha$  ([Rao & Turnshek 2000; Rao et al. 2006; Rao et al. 2017](#)). In such studies, the selection biases are difficult to quantify and the limited sample size results in the cosmic H I mass density remaining poorly constrained. Alternatively, blind surveys for DLAs in the UV spectra of quasars avoid potential biases ([Neeleman et al. 2016](#)), but are statistically limited by the small number of detections.

Analogous to Lyman- $\alpha$  studies in the spectra of quasars, the 21-cm H I absorption line is a useful tool for tracing neutral gas in the distant Universe. While methodologically similar (i.e. using a background source to probe sightlines through gas), absorption in the radio is weighted towards the coldest ( $T_s \sim 100$  K) H I and assumptions in the spin temperature are required to obtain a total column density. Unlike H I emission studies, absorption line spectroscopy is not limited by redshift, but rather the intensity of the background source. However, blind surveys of 21-cm absorption have thus far been limited by poor spectral bandpass and terrestrial radio-frequency interference ([Brown & Mitchell 1983; Darling et al. 2004](#)). It is only with the recent construction of SKA pathfinder telescopes Australian Square Kilometre Array Pathfinder (ASKAP) ([Johnston et al. 2007; DeBoer et al. 2009](#)) and Meer Karoo Array Telescope (MeerKAT) ([Jonas & MeerKAT Team 2016](#)), with wide-band correlators and locations in radio-quiet sites, that these limitations are overcome.

The First Large Absorption Survey in H I (FLASH, Allison et al., in preparation) is a blind, all-sky survey using the ASKAP radio telescope to search for neutral gas systems. ASKAP comprises 36 12-m antennas equipped with novel phase array feed technology and possesses a 30 deg $^2$  field-of-view ([Hotan et al. 2021](#)). The FLASH project will search for H I absorption in the largely unexplored redshift range  $0.4 < z < 1.0$  and commissioning and early science results have already yielded several new detections ([Sadler et al. 2020; Allison et al. 2020](#)). Such blind surveys for neutral hydrogen are unaffected by dust obscuration ([Pontzen & Pettini 2009; Krogager et al. 2019](#)) and biases potentially induced by spectroscopic pre-selection of targets using the Mg II absorption line ([Neeleman et al. 2016](#)).

While 21-cm absorption line spectroscopy is a powerful technique for probing the neutral gas content of galaxies, it provides only a single sightline through systems. The origin of the gas detected in intervening systems remains unclear without follow-up imaging as the galaxy or galaxies associated with the neutral gas cannot be identified. Integral-field spectroscopy (IFS) provides both spectra and imaging for objects in a field and allows efficient identification of galaxies associated with the absorbing gas. The technique of com-

binning UV absorption spectroscopy with IFS observations in the near-infrared has been applied at redshifts  $z \sim 1$  and  $z \sim 2$  with the SINFONI instrument ([Bouché et al. 2007; Péroutx et al. 2011, 2013](#)). This allows properties such as the SFR, gas kinematics and metallicity of these systems to be analysed and used to interpret the physical behaviour of the gas seen initially in absorption (i.e. outflows, inflows or co-rotation with halo). More recently, the MusE GAs FLOW and Wind (MEGAFLOW) survey have compared the properties of the gas traced by Mg II absorption with the kinematics, stellar masses, star formation rates (SFRs) and orientation of their associated galaxies at  $z \approx 1$  to investigate gas accretion and galactic winds ([Schroetter et al. 2019; Zabl et al. 2019](#)). The MUSE-ALMA Halos Survey study the environments of strong H I absorbers at  $z \leq 1.4$  and reveal an increasing number of galaxy groups associated with a single absorber ([Péroutx et al. 2016, 2019; Klitsch et al. 2017; Rahmani et al. 2018; Hamanowicz et al. 2020](#)). These studies, using the complementary methods of absorption and 3D spectroscopy, reveal that the environment of absorbers is often complex and larger, more representative samples are necessary to understand the cycling of gas in these systems.

Thus far, absorbers at  $0.2 \leq z \leq 1.7$  have column densities measured using the Lyman- $\alpha$  line in the UV spectra of quasi-stellar objects (QSOs), which results in a rather limited sample for follow-up imaging and spectroscopy. We expect to detect  $\sim 1000$  21-cm absorbers with the FLASH project, providing an enormous sample of absorbers that allow us to examine the relationship between the galaxy environment and neutral gas behaviour at an epoch with limited observational constraints. Moreover, in contrast to previous studies that use the Mg II doublet in absorption to trace gas that is  $T \sim 1000$  K in the circumgalactic medium (CGM), H I absorption in the radio traces cold neutral gas that is required for star formation. Mapping how the coldest neutral gas cycles in the CGM of galaxies enables us to directly explore the effects of accretion, outflows and interactions on star formation in galaxies. Here, we present new MUSE observations of galaxies associated with a 21-cm DLA at  $z_{\text{abs}} = 0.4503$  detected from a ASKAP commissioning project towards QSO PKS 1610-771 ([Sadler et al. 2020](#)). Section 2 presents the initial H I detection and relevant ancillary observations. Details of the data processing and additional sky corrections for the new MUSE observations are found in section 3. In section 4, we analyse the MUSE observations and identify objects in the field associated with the absorber. Finally, we discuss the physical nature of the gas detected with ASKAP in section 5. In this paper, we adopt a flat- $\Lambda$ CDM cosmology, with parameters  $H_0 = 70$  km s $^{-1}$  Mpc $^{-1}$ ,  $\Omega_\Lambda = 0.7$  and  $\Omega_m = 0.3$ .

## 2 THE FIELD OF PKS 1610-771

### 2.1 ASKAP Detection of 21-cm absorption

The radio data for the neutral hydrogen detection towards the quasar PKS 1610-771 were initially taken using the six-antenna Boolardy Engineering Test Array (ASKAP-BETA) ([Hotan et al. 2014; McConnell et al. 2016](#)) in the period July 2014 to February 2016. During commissioning time with the ASKAP Early Science array (ASKAP-12 [Hotan et al. 2021](#)),

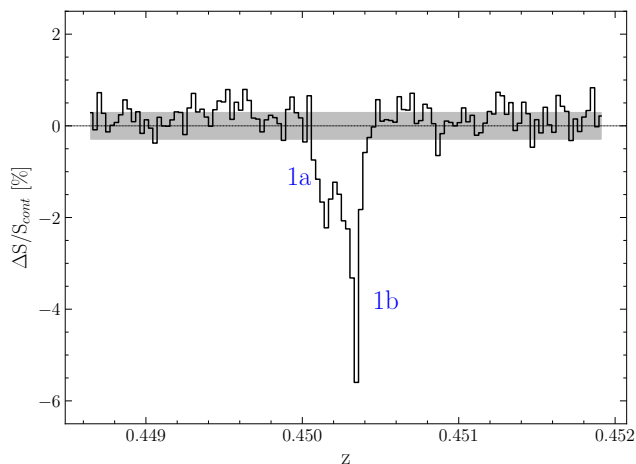


**Figure 1.** 21-cm H I absorption-line profile along the line of sight to the bright radio source PKS 1610-771. The light grey band indicates the  $1\sigma$  limit in optical depth. There are two distinct velocity components (labelled 1a and 1b) that are  $43 \text{ km s}^{-1}$  apart. The spectrum is reproduced

from Sadler et al. (2020).

the absorber was re-observed with greater sensitivity (rms noise  $12.7 \text{ mJy}$  per channel compared to  $16.5 \text{ mJy}$  per channel for BETA) in January - February 2017. In total, PKS 1610-771 was observed for 7 hours using ASKAP-BETA and ASKAP-12. These observations were part of a FLASH pilot study towards bright ( $20 \text{ GHz}$  flux density above  $0.5 \text{ Jy}$ ) and compact radio sources (Sadler et al. 2020) without pre-selection based on criteria such as Mg II absorption. For both observations, the frequency resolution was  $18.5 \text{ kHz}$ , corresponding to a velocity resolution of  $5.7 \text{ km s}^{-1}$  in the rest-frame.

The 21-cm absorber detected towards PKS 1610-771 has APPROXIMATE redshift  $z_{\text{abs}} = 0.4503$ . As can be seen from Figure 1, there are two components  $43 \text{ km s}^{-1}$  apart in radial velocity. Very-long-baseline interferometry (VLBI) imaging of the quasar at  $8.4 \text{ GHz}$  reveals emission that is extended  $5 \text{ mas}$ , equivalent to roughly  $30 \text{ pc}$  at  $z_{\text{abs}} = 0.4503$  (Ojha et al. 2010). In calculating the column density of the neutral hydrogen, we assume a covering factor  $f = 1$  because the projected size of the background source at the absorber redshift is smaller than the typical size of H I clouds ( $\gtrsim 100 \text{ kpc}$ , Braun 2012). The resulting H I column density assuming the fiducial spin temperature of  $100 \text{ K}$  is  $N_{\text{H I}} = 2.7 \pm 0.1 \times 10^{20} \cdot [T_s/100\text{K}] \cdot \text{cm}^{-2}$ . As the optical depth of the 21-cm line is inversely proportional to spin temperature, and the harmonic mean spin temperature of galactic H I is  $\sim 300 \text{ K}$  (Murray et al. 2018), we expect the absorber to be a DLA ( $N_{\text{H I}} > 2 \times 10^{20} \text{ atoms cm}^{-2}$ ). We tabulate the redshifts and column densities of the individual Gaussian components required to fit the absorption profile returned from a Bayesian detection method (Allison et al. 2012) in Table 1.

**Table 1.** Model parameters derived from fitting H I absorption towards PKS 1610-771 for the combined spectrum after 7 hours of observations with both BETA and ASKAP-12. Column 1 gives the Gaussian component corresponding to Figure 1; column 2 the redshift; column 3 the log of the H I column density ( $T_s = 100\text{K}$ ,  $f = 1$ ); column 4 the velocity FWHM for the optical depth; column 5 the peak component depth normalised by the continuum flux density. The errors for each parameter are determined using the 1 standard deviation from their marginal posterior distributions calculated using MCMC (Allison et al. 2012).

ID	$z$	$\log_{10} N_{\text{H I}}$ [ $\text{cm}^{-2}$ ]	$\text{dv}$ [ $\text{km s}^{-1}$ ]	$(\Delta S/S_{\text{cont}})_{\text{peak}}$ %
(1)	(2)	(3)	(4)	(5)
1a	$0.450184^{+0.000014}_{-0.000014}$	$20.3^{+0.6}_{-0.6}$	$47^{+5}_{-6}$	$0.0194^{+0.0012}_{-0.0012}$
1b	$0.4503276^{+0.0000016}_{-0.0000015}$	$20.0^{+0.6}_{-0.5}$	$11.2^{+1.5}_{-1.1}$	$0.045^{+0.003}_{-0.003}$

## 2.2 Ancillary Observations of the PKS 1610-771 field

The quasar PKS 1610-771 was first observed by Courbin et al. (1997) as a suspected gravitational lens with the New Technology Telescope (NTT) in 1995. Imaging centred on the quasar revealed four galaxy-like objects (referred to as objects A, B, C & D) within a few arcseconds of the quasar, with object D only visible after a 2D PSF subtraction of the QSO light.

Early spectroscopic observations of PKS 1610-771 reveal that this quasar is highly reddened (Hunstead & Murdoch 1980; Courbin et al. 1997), implying that there is significant dust absorption in the host galaxy of the quasar or in intervening galaxies along the line of sight. Such a reddened QSO may be excluded from optical DLA samples (Krogager et al. 2019), which highlights how 21-cm H I surveys without pre-selection can overcome selection biases related to dust.

More recent spectroscopic observations of objects A (impact parameter  $8.8 \text{ kpc}$ ) and B (impact parameter  $17.8 \text{ kpc}$ ) with the 8-m Gemini-South telescope revealed them to be galaxies whose redshifts fell within  $100 \text{ km s}^{-1}$  of the neutral gas detected by ASKAP (Sadler et al. 2020). While this suggests that the H I absorption is likely to be associated with one of these galaxies, the exact nature and origin of the H I gas seen in absorption remained unclear.

## 3 MUSE OBSERVATIONS OF THE PKS 1610-771 FIELD

MUSE observations of the galaxy group were taken centred on the quasar PKS 1610-771 for a total of three hours on source. They were carried out in service mode (programme 0103.A-0656, PI: E. Sadler) in three separate ‘observing blocks’ (OBs) on the nights of 2019 April 12, May 8 and 9. Each observing block was divided into two sub-exposures ( $T_{\text{exp}} = 2 \times 1800 \text{ s}$ ) with a  $90^\circ$  rotation and a sub-arcsec dithering pattern was applied between these to minimise artefacts and obtain more uniform noise properties in the dataset. The field-of-view was  $60 \text{ arcsec} \times 60 \text{ arcsec}$  with a  $0.2 \text{ arcsec/pixel}$  scale using the Wide Field Mode and the instrument’s ‘nominal mode’ used has a spectral coverage spanning  $4800 - 9300 \text{ \AA}$ . At the redshift of the intervening H I gas  $z_{\text{abs}} = 0.4503$ , this covers strong emission lines from [O II] to [O III]. The GALACSI Adaptive Optics (AO) system

was used to improve the seeing. This AO system consists of four artificial sodium Laser Guide-Stars to correct for atmospheric turbulence at the cost of blocking  $\sim 200$  Å centred around the Na I D line to prevent contamination and saturation of the detector. Consequently, the H $\delta$  line at the DLA redshift is not covered, but stronger Balmer lines (H $\beta$  and H $\gamma$ ) are available in the wavelength coverage.

The raw MUSE exposures were reduced using version 2.6.2 of the ESO MUSE pipeline and associated static calibrations (Weilbacher et al. 2016). Each raw exposure was corrected using master bias, flat-field and arc lamp exposures based on data taken closest in time to the science observations. The MUSE line-spread functions (LSF) part of the pipeline package were used as the parameters of the LSF are considered stable. The raw exposures were then processed with the SCIBASIC recipe, using the above calibrations to remove the instrument signature. During the removal of the sky background with SCIPOST, corrections for the Raman scattered light from the lasers were made and a barycentric reference was adopted to make sure the wavelength calibration was consistent with the ASKAP data. These individual exposures were then aligned using EXP\_ALIGN to ensure accurate astrometry and then finally combined using the EXP\_COMBINE recipe.

The data reduction pipeline (v 2.6.2) for MUSE has sub-optimal sky subtraction that leaves artifacts in the final product. Given the faintness of some of the targets, it becomes essential to remove these sky residuals to obtain usable spectra. The PCA-based method from Husemann et al. (2016) was found to be effective and it significantly improved the final sky subtraction. PCA components were created for regions of sky selected by the user and then applied to the data cube. This yielded better quality spectra than the original pipeline product and are presented here. The known wavelengths of the OH night sky emission lines (5577 & 6300 Å) were used to check the wavelength calibration by turning off the sky subtraction for an exposure. Using this method, the wavelength solution was found to be accurate to 20 km s<sup>-1</sup>. The resulting point spread function (PSF) measured from bright sources near the field centre using a Moffat profile has a FWHM of 0.68 arcsec at 7000 Å.

## 4 ANALYSIS AND RESULTS

### 4.1 Associated Galaxies

Figure 2 depicts a pseudo narrow-band (NB) image centred around the [O II] lines at the redshift of the absorber  $z_{\text{abs}} = 0.4503$ . It reveals four objects with [O II] emission near  $z_{\text{abs}} = 0.4503$  and these are marked in red (A, B, X and Y). In addition to galaxies A and B, which were known to be associated with the DLA from spectroscopy (Sadler et al. 2020), we find another two galaxies (X and Y) with impact parameters of 136 and 190 kpc respectively from the QSO sightline. This galaxy group is aligned in what may be a filamentary structure extending from north-east to south-west.

As NB images may miss passive galaxies without emis-

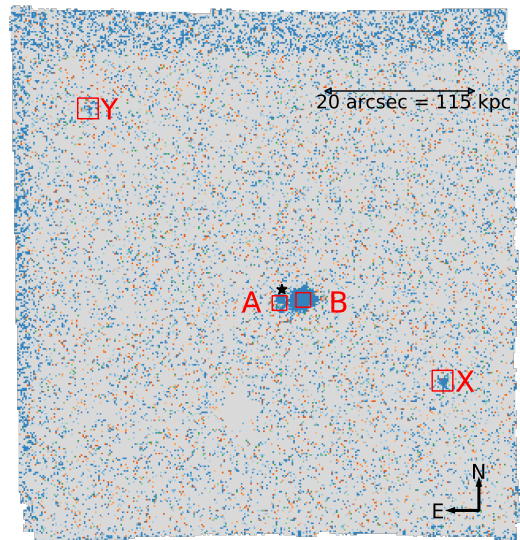


**Figure 2.** Pseudo narrow-band image with width 1000 km s<sup>-1</sup> around [O II] doublet at  $z_{\text{abs}} = 0.4503$ . Orientation is north-east (up-left). Galaxies associated with the H I 21-cm absorber have been marked in red, and the centre of quasar PKS 1610-771 by a black star. In addition to objects A and B, we find two galaxies (labelled X and Y) with projected distances more than 150 kpc from the absorber. The position of the group members is reminiscent of a filamentary structure stretching from galaxy Y (north-east) to galaxy X (south-west).

sion nebulae, the PROFOUND<sup>1</sup> algorithm (Robotham et al. 2018) is used to identify sources in the field and extract spectra. From the final segmentation map generated (see Robotham et al. 2018, for detailed method), redshifts are obtained using the QXP<sup>2</sup> (Davies et al. in prep.) package in R. Due to various overlapping sources such as QSO PKS1610-771 and galaxy A, this results in several misidentifications, which are corrected for manually. The MUSE Line Emission Tracker (MUSELET) module of the MPDAF<sup>3</sup> package (Bacon et al. 2016) is also used to systematically search for emission-line galaxies at the redshift of the DLA. Combined with PROFOUND and a visual inspection, a complete search for associated galaxies was performed down to the detection limit  $\sim 23$  mag. The resulting white-light image in Figure 3 contains 84 marked sources, of which only the four marked in red have measured redshifts within 1000 km s<sup>-1</sup> of the absorber at  $z_{\text{abs}} = 0.4503$ . These four galaxies form a galaxy group with velocity dispersion 270 km s<sup>-1</sup>.

Objects C and D (Courbin et al. 1997) detected at low angular separation to the quasar are not found to be associated with the absorber. The former is found to be a faint M-type star at  $z \sim 0$  from its prominent TiO bands (see Figure A1 for the spectrum). Object D is obscured by the point spread function of the bright quasar. Horizontal and vertical slices across the expected position of galaxy D are initially

<sup>1</sup> [github.com/asgr/ProFound](https://github.com/asgr/ProFound)

<sup>2</sup> <https://github.com/lukejdavies/FourXP>

<sup>3</sup> <https://mpdaf.readthedocs.io/en/latest/index.html>



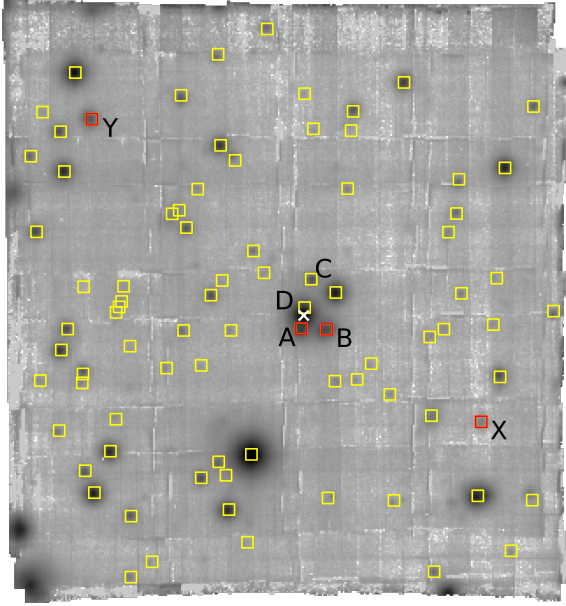


**Figure 3.** Overlaid on a white-light image of the field are all identified objects, with the quasar PKS 1610-771 at the centre marked by a white cross. Galaxies detected within  $1000 \text{ km s}^{-1}$  of the H I 21-cm absorber have been marked in red, while other objects in the field are marked in yellow. Sources near the edge of the field are not identified. North is up and east is left.

used to determine candidate emission lines by visually inspecting changes in the spectrum of the quasar. Then, a spectral PSF subtraction (Hamanowicz et al. 2020) is used to reveal these obscured lines. We note that this method does not allow extraction of the object’s continuum. Potential emission lines are found near  $5587 \text{ \AA}$  and  $7290 \text{ \AA}$  (see Figure A2), corresponding to [O II] and H $\beta$  at  $z = 0.5001$ . Although the possible [O II] line is very near the  $5577 \text{ \AA}$  sky emission line, Hunstead & Murdoch (1980) observed a similar emission feature near  $5590 \text{ \AA}$  four decades prior. The H $\beta$  emission at  $7290 \text{ \AA}$  is well-supported by the shifting centroid of the line across spaxels, signifying rotation of the ionized gas, and this places galaxy D near  $z = 0.5$ . We note that upon inspection of individual exposures, these lines do not consistently appear. Regardless, there is no evident emission from strong lines such as [O II], [O III] and H $\beta$  near  $z_{\text{abs}} = 0.4503$  in front of the quasar and hence, the absorber is likely not associated with object D.

The positions and redshifts of the galaxies associated with the DLA at  $z_{\text{abs}} = 0.4503$  are tabulated in Table 2. For galaxies A and B, the continuum emission is clear and there is evident Ca II H&K and Na I D absorption. The remaining galaxies (X and Y) have faint continuum emission, but Ca II absorption is still present. Emission lines [O II] and H $\beta$  can be seen in all four group members as seen in Figure 4, with H $\gamma$  also prominent in galaxies B and Y. Figure 5 reveals that the spectra of galaxies A, B and Y also feature higher-order Balmer lines (H $\epsilon$ , H $\zeta$ , H $\eta$ , H10, H11 and H12). While analysis of the underlying stellar population for these galaxies is difficult due to the low signal-to-noise ratio (S/N),

the lines reveal the presence of a significant population of A-type stars. Indeed, this is supported by fits using the Penalized Pixel-Fitting software PPXF<sup>4</sup> v7.0.0 (Cappellari & Emsellem 2004; Cappellari 2017) and MILES stellar library (Sanchez-Blazquez et al. 2006; Falc3n-Barroso et al. 2011), where A-type stars are among the highest weighted stellar templates for the three galaxies.

## 4.2 Star Formation Rates

The star formation rate of each galaxy group member can be estimated from the integrated flux of the [O II] emission line. For galaxies A, X and Y, the empirical relation in Kennicutt (1998) without an extinction correction is used:

$$\text{SFR} = (1.4 \pm 0.4) \times 10^{-41} L([\text{O II}]) \text{ M}_{\odot} \text{ yr}^{-1}. \quad (1)$$

Due to the availability of prominent H $\beta$  and H $\gamma$  lines in the spectrum of galaxy B, the [O II] luminosity can be corrected for reddening. An intrinsic H $\gamma$ /H $\beta$  = 0.47 Balmer decrement is assumed (Osterbrock 1989) to determine the emission-line colour excess and using the Kewley et al. (2004) relation, a SFR of  $4.3 \text{ M}_{\odot} \text{ yr}^{-1}$  is calculated for galaxy B. The other galaxies associated with the absorber have H $\gamma$  emission nebulae with fluxes that are highly uncertain due to poor S/N or are below the detection limit. While galaxies A, X and Y are passive with SFRs  $\lesssim 0.5 \text{ M}_{\odot} \text{ yr}^{-1}$ , galaxy B has a star formation rate larger by roughly an order of magnitude. The resulting values are in Table 3.

## 4.3 Gas Kinematics

### 4.3.1 Neutral Gas

In the MUSE spectrum of QSO PKS 1610-771 at  $z = 1.71$ , there are various metal absorption lines. A closer inspection reveals that these lines belong to two separate systems at redshifts  $z \sim 0.45$  and  $z \sim 1.61$  (see Figure C1). We focus on the  $z \sim 0.45$  system consisting of low ionisation potential metal lines Na I D<sub>1</sub> & D<sub>2</sub> and Ca II H & K as the DLA is found at  $z_{\text{abs}} = 0.4503$ . VPFIT v10.4 (Carswell & Webb 2014) is used to fit the doublets after converting the MUSE spectrum to vacuum wavelengths and two components are found to be necessary for the line profile. This is in agreement with a visual inspection of the line profiles, where there is an extended wing in the Ca II K absorption feature and the Na I D doublet appears double-peaked (Figure 6).

In the intergalactic environment of the Milky Way, these ions generally trace extraplanar high-velocity clouds with H I column densities ranging from  $10^{17}$  to  $10^{20} \text{ cm}^{-2}$  (Richter et al. 2005; Bekhti et al. 2008). Similarly, we find from Voigt profile fits of these ions that the redshift of the higher column density component aligns with the velocity of the neutral gas detected by ASKAP. However, we see in Figure 6 that there is a second fitted component, redshifted  $180 \text{ km s}^{-1}$  from the former. An examination of the 21-cm absorption line in Figure 1 reveals there is no corresponding feature near  $z = 0.4509$ , suggesting the gas probed is of lower H I column density or higher spin temperature. Regardless, the MUSE data has uncovered another component to the absorber.

<sup>4</sup> <https://pypi.org/project/ppxf/>

**Table 2.** Position of galaxies with redshifts within  $1000 \text{ km s}^{-1}$  of the DLA. Column 1 gives the ID marked in the white-light image of Figure 3; column 2 the right ascension; column 3 the declination; column 4 the angular separation in arcsec; column 5 the impact parameter in kpc; column 6 the redshift; column 7 the velocity with respect to the peak of the H I absorber.

Galaxy	RA	DEC	$\delta$	$b$	$z$	$v_{\text{DLA}}$
(1)	(2)	(3)	(4)	(5)	(6)	(7)
A	16:17:48.29	-77:17:24.72	1.53	8.82	0.45061	$93 \pm 20$
B	16:17:47.40	-77:17:24.81	3.08	17.76	0.45038	$24 \pm 20$
X	16:17:42.06	-77:17:35.34	23.61	136.04	0.45129	$297 \pm 20$
Y	16:17:55.52	-77:17:00.83	32.95	189.86	0.45279	$747 \pm 20$

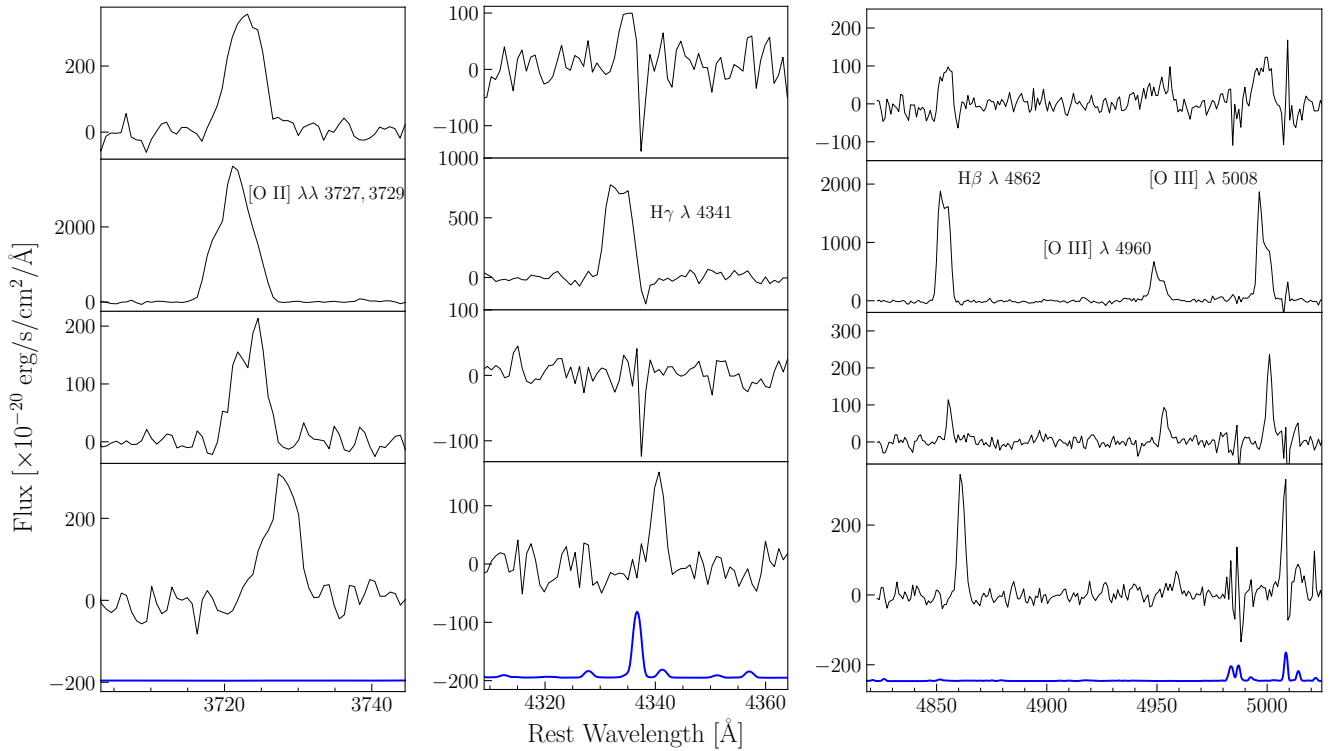


**Figure 4.** Emission lines for galaxies A, B, X and Y from top to bottom. Included are [O II], H $\gamma$ , H $\beta$  and [O III]. The continuum-subtracted spectrum is in black with the vertically offset and arbitrarily scaled sky spectrum in blue (bottom panel). Residuals from subtraction of night sky lines near  $6300 \text{ \AA}$  and  $7200 - 7300 \text{ \AA}$  affect integrated flux measurements for the H $\gamma$  and [O III] doublet emission lines.

**Table 3.** Emission line fluxes and star formation rates for members of the galaxy group. Column 1 gives the galaxy ID; column 2 the [O II] flux; column 3 the H $\gamma$  flux; column 4 the H $\beta$  flux; columns 5 and 6 the [O III] 4960 Å and 5008 Å fluxes respectively; column 7 the star formation rate.

Galaxy	$F([\text{O II}])$	$F(\text{H}\gamma)$	$F(\text{H}\beta)$	$F([\text{O III}])$	$F([\text{O III}])$	SFR
(1)	(2)	(3)	(4)	(5)	(6)	(7)
A	$(5.1 \pm 1.7) \times 10^{-17}$	—	$(1.1 \pm 0.2) \times 10^{-17}$	—	$(1.8 \pm 0.4) \times 10^{-17}$	$0.55 \pm 0.18$
B	$(52 \pm 8) \times 10^{-17}$	$(9 \pm 2) \times 10^{-17}$	$(23 \pm 4) \times 10^{-17}$	$(7 \pm 2) \times 10^{-17}$	$(17 \pm 4) \times 10^{-17}$	$4.3 \pm 1.1^a$
X	$(2.4 \pm 1.0) \times 10^{-17}$	—	$(0.6 \pm 0.3) \times 10^{-17}$	$(0.6 \pm 0.3) \times 10^{-17}$	$(1.5 \pm 0.6) \times 10^{-17}$	$0.26 \pm 0.11$
Y	$(4.1 \pm 1.7) \times 10^{-17}$	$(0.9 \pm 0.5) \times 10^{-17}$	$(2.5 \pm 1.1) \times 10^{-17}$	—	$(1.6 \pm 1.2) \times 10^{-17}$	$0.44 \pm 0.18$

<sup>a</sup> Corrected for extinction.

#### 4.3.2 Ionized Gas

Absorption-line studies probe pencil-beam sightlines towards the background source and allow statistical studies of the neutral gas amount and distribution at intermediate redshifts (e.g. Sadler et al. 2020). However, the interpretation of the H I kinematics requires further optical spectroscopy and imaging of associated galaxies. To unravel the relationship

between the neutral gas and the galaxy group, it becomes essential to analyse the absorber velocity relative to the stellar or ionized gas kinematics of galaxies A, B, X and Y. The S/N of the stellar continuum is too low ( $< 3$ ) in individual spaxels to measure the line-of-sight velocity distribution (LOSVD) for stars reliably. Instead, we use PPXF to derive the LOSVD for the ionized gas and generate velocity maps.

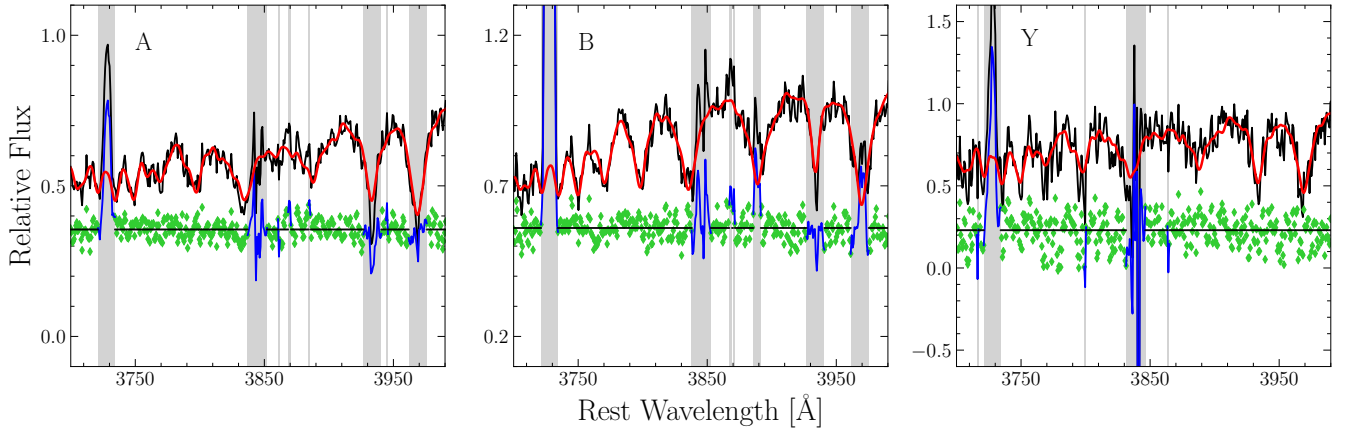


**Figure 5.** Spectra of higher-order Balmer lines for galaxies A (left), B (centre) and Y (right) at the rest wavelength. The original spectrum is in black with template

fits from PPXF overlaid in red. The grey shaded areas indicate regions that have been masked during fitting – these correspond to emission lines (e.g. [O II]), the 5577 Å sky line and other regions with strong sky residuals. In green are the residuals that are vertically offset from the black horizontal line and the masked residuals are in blue.

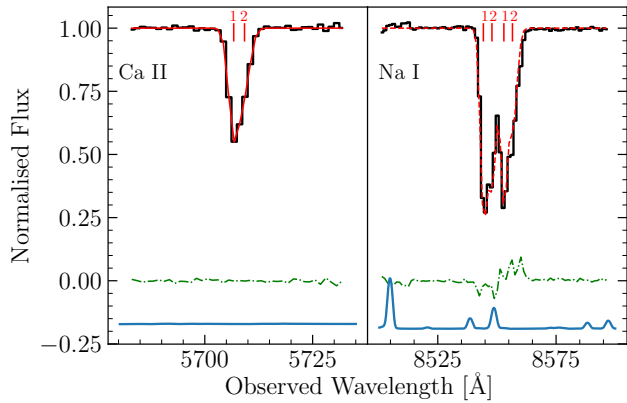


**Figure 6.** Normalised MUSE spectrum of Ca II K (left) and Na I doublet (right) in front of QSO PKS 1610-771. The spectrum is plotted in black with Voigt fits in red and residuals in green. There are two components for both ions, most clear in the Na I fit. The first component coincides with the redshift from ASKAP near  $z_{\text{abs}} = 0.4503$ , while the weaker component is at redder wavelength. The sky spectrum is in blue.

Only the emission lines of galaxy B meet the signal-to-noise ratio cutoff  $S/N > 3$  for a significant number of individual spaxels and the remaining galaxies in the group cannot have their ionized gas mapped.

[O II] and H $\beta$  are the emission lines used to create the rotational velocity map in Figure 7 as they are the strongest lines in the spectrum, allowing more accurate measurements in the outskirts of the disc. All velocities are represented relative to galaxy B’s systemic redshift. This is calculated by applying a further correction to the original MARZ fit using PAFIT (Krajinović et al. 2006) on an ionized velocity map of the galaxy and is found to be within  $15 \text{ km s}^{-1}$  of the central velocity measured by GALPAK<sup>3D</sup> (Bouché et al. 2015). Galaxy A is included to illustrate its projected position and relative velocity. Velocities of the neutral gas

are also included near the expected position of the absorber for comparison to galaxy B’s rotating disc. The PSF FWHM of 0.68 arcsec at 7000 Å is represented in the bottom left of Figure 7 by the diameter of the circle.

## 5 RELATIONSHIP BETWEEN THE NEUTRAL GAS AND GALAXY GROUP

In total, we have three kinematic measurements of the neutral gas at  $z \sim 0.45$ . Two velocities are derived directly from the components of the initial ASKAP detection (Figure 1) and a third by proxy using the low-ionisation metal absorption lines Na I and Ca II (Figure 6). Due to the overlap in redshift between the ASKAP H I detection and component ‘1’ from the MUSE spectra, they are likely tracing the same gas. We henceforth only consider the 21-cm components because ASKAP has a significantly better velocity resolution of  $5.7 \text{ km s}^{-1}$  at  $z_{\text{abs}} = 0.4503$  compared to  $\sim 110 \text{ km s}^{-1}$  at 7000 Å for MUSE. If the metal lines are indeed tracing the neutral gas, the distinct components seen in the radio are possibly not resolved in the MUSE data and hence, appear as a single component. The three components will be henceforth referred to as 1a, 1b and 2 in order of increasing redshift and their properties are listed in Table 4.

With the relevant neutral gas velocities identified and associated galaxies analysed, we can now try to understand the relationship between the gas and surrounding group. In Figure 8, the impact parameters and redshifts of galaxies A, B, X and Y are compared to the velocities of the gas seen in absorption by both ASKAP and MUSE. Galaxies A and B have the smallest projected separations to the absorber and are closest to it in velocity space. Since the 21-cm absorber detected with ASKAP has DLA-equivalent column density, there are restrictions on which galaxies are directly related to the neutral gas in front of the quasar. The characteristic radius of 21-cm DLA sources is estimated to be less than 20 kpc from studies at lower redshift (Borthakur 2016; Reeves et al. 2016; Curran et al. 2016; Dutta et al. 2017),

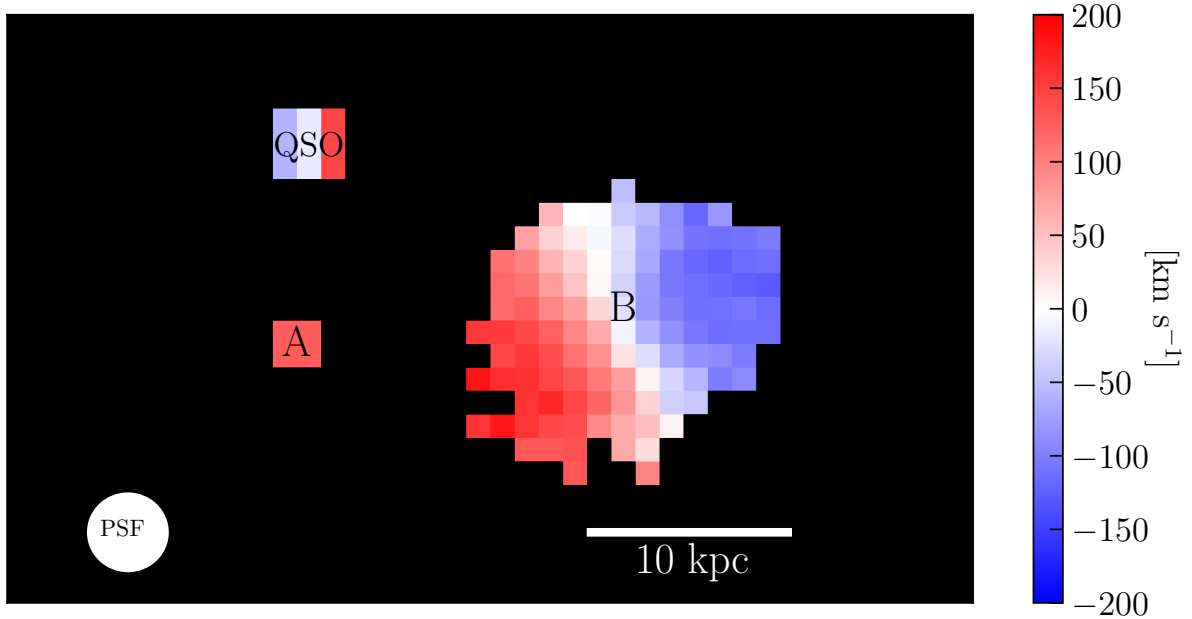


**Figure 7.** Kinematic map of the ionized gas in galaxy B, with zero velocity at its systemic redshift. At the position of the QSO PKS 1610-771, the three vertical stripes correspond to the neutral gas velocities along the quasar sightline. The blue and white stripes reflect the velocities of the two H I components measured with ASKAP, while the red stripe is from Voigt profile fitting of the Ca II and Na I doublets. The position of galaxy A is marked with a single velocity corresponding to its systemic redshift. At the bottom left is a circle with diameter equivalent to the FWHM of the seeing at 7000 Å. The spatial sampling is 0.2 arcsec/pixel, corresponding to 1.15 kpc/pixel at  $z_{\text{abs}} = 0.4503$ .

**Table 4.** Properties of the three gas components considered. Components 1a and 1b are taken from the ASKAP detection, while component 2 at higher redshift is obtained from fitting low-ionisation ions in the MUSE spectrum of the quasar. Column 1 is the component ID; column 2 the redshift of the component; columns 3 and 4 the velocities of the component with respect to the systemic redshift of galaxies A and B respectively; column 5 the absorption lines associated with each component.

Component	$z$	$v_A$ [km s <sup>-1</sup> ]	$v_B$ [km s <sup>-1</sup> ]	Lines
(1)	(2)	(3)	(4)	(5)
1a	0.45018	-128	-16	H I, Ca II, Na I <sup>a</sup>
1b	0.45033	-85	-59	H I, Ca II, Na I
2	0.4509	+96	+150	Ca II, Na I

<sup>a</sup> Ca II and Na I component near  $z = 0.4503$  in MUSE spectrum could trace both ASKAP H I components due to insufficient velocity resolution.

constraining the source of the H I to be at a similar impact parameter. We hence exclude galaxies X and Y from having a direct relation to the DLA given their large projected separation (136 and 189 kpc respectively) compared to galaxies A and B, which have impact parameters  $< 20$  kpc. Further discussion revolves around this pair of galaxies nearest the quasar sightline.

### 5.1 Co-rotation with Disc

The size of the H I disc in isolated galaxies is roughly twice the optical diameter (e.g. Rao & Briggs 1993; Boomsma et al. 2008). Thus, the absorber is possibly probing gas co-rotating with a galaxy, and this can be tested by extrap-

olating from the kinematics of the ionized disc determined using PPXF. The low S/N of the emission lines in galaxy A and its compact nature render determining a reliable rotation map impossible. Therefore, our discussion focuses on galaxy B, which has resolved rotation.

From Figure 7, we see that the redshifted side of galaxy B is orientated towards the QSO sightline. Thus, components 1a ( $-57 \text{ km s}^{-1}$ ) and 1b ( $-15 \text{ km s}^{-1}$ ) corresponding to the velocities of the H I detection from ASKAP are not consistent with galaxy B’s rotating disc even after accounting for uncertainties in redshift measurements. Component 2 from the Na I and Ca II is consistent with this phenomenon as it is also redshifted with respect to the systemic velocity of galaxy B. Given that there is no corresponding H I absorption for component 2, the neutral gas may be warmer, and this is consistent with the 21-cm line being more sensitive to cold neutral hydrogen. This component may be tracing gas in the outer disc of galaxies heated by the radiation field. However, other processes are required to account for the kinematics of the ASKAP H I detection.

### 5.2 Outflows

In current models, outflows are expected to be preferentially aligned with a galaxy’s minor axis as enhanced resistance along the galactic plane effectively collimates outflows into a biconical shape (Nelson et al. 2019; Péroux et al. 2020). The azimuthal angle  $\alpha$ , defined as the angle between the galaxy major axis and projected position of the quasar, is typically used to distinguish between accretion and winds (e.g. Zabl et al. 2019; Schroetter et al. 2019). For galaxy B,



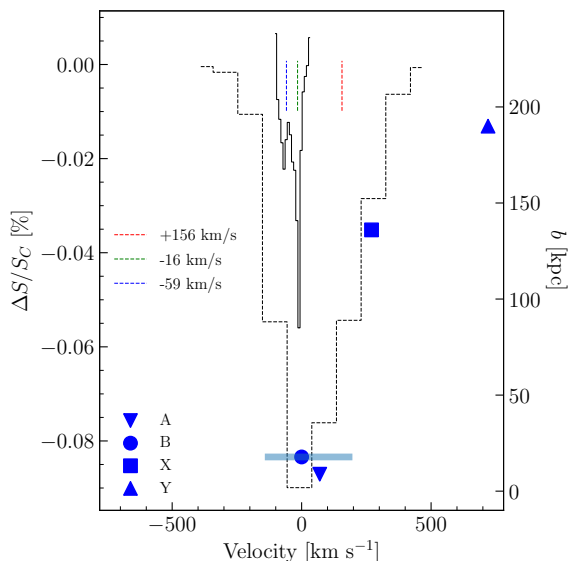


**Figure 8.** The ASKAP H I absorption line profile in velocity space is plotted in black with the velocities of its two components labelled by the dashed blue (1a) and green (1b) lines. This spectrum is to scale and plotted against the fraction of absorbed background continuum  $\Delta S/S_C$ . The dashed spectrum is Ca II K absorption from MUSE and has its second component marked in red (2). Note that the first component of the Ca II K metal line aligns with the ASKAP components and is not plotted. Each of the galaxies are represented by blue markers using their respective redshifts and impact parameters to the gas in kpc ( $b$ , right axis). At the position of galaxy B, a horizontal line marks the extent of its rotation. All velocities are with respect to the systemic redshift of galaxy B ( $z = 0.45038$ ) to be consistent with Figure 7.

it is found that  $\alpha = 57^\circ$  which indicates that the absorber is preferentially aligned with the minor axis. Combining this alignment with the high SFR of galaxy B ( $4.3 M_\odot \text{ yr}^{-1}$ ) means stellar winds driving out neutral gas is a possibility. Galaxy A has too low S/N emission lines in individual spaxels to be modelled using GALPAK<sup>3D</sup>, and its proximity to the quasar prevents accurate measurements of its photometric position angle. Galaxies X and Y are unlikely candidates due to their  $> 100$  kpc impact parameter to the DLA and large velocity difference of  $+297$  and  $+747 \text{ km s}^{-1}$  respectively to the absorber redshift. If outflowing gas is responsible for the absorption features, it is far more likely that the winds originate from galaxy B due to its proximity and high SFR.

However, the high H I column densities of components 1a and 1b suggest that cold dense neutral gas is being traced. While galactic winds are seen to be ubiquitous at all redshifts, an important consideration is whether the outflowing cold gas can survive out to  $\sim 20$  kpc from galaxy A or B without breaking down or being heated and ionized. Simulations predict starburst-driven outflows to be multi-phase, consisting of a hot and fast ionized component entraining colder gas from the interstellar disc (Veilleux et al. 2005). More recent hydrodynamical simulations suggest mechanisms for the cold gas to accelerate to wind speeds and grow in mass (Gronke & Oh 2018, 2020). Outflows of low-ionized gas traced using Mg II absorption have been seen to extend beyond 100 kpc (e.g. Schroetter et al. 2019), but this

traces gas at temperatures of  $\sim 1000$  K. Despite this, outflowing H I may be too hot ( $T > 1000$  K) to be detected by 21-cm absorption given the strong dependence of optical line depth on spin temperature. Assuming a mean harmonic spin temperature of 1000 K for our absorber requires an order of magnitude increase in the H I column density ( $N_{\text{HI}} = 2.7 \pm 0.1 \times 10^{21} \text{ atoms cm}^{-2}$ ) to reproduce the observed absorption line. This means that it is unlikely components 1a and 1b are a result of galactic winds.

Outflows of cool gas have been observed at higher redshift in other galaxies using Na I D absorption against background stellar continuum (so-called ‘down-the-barrel’ spectroscopy, e.g. Heckman et al. 2000; Cazzoli et al. 2016). While the detected outflow regions in these studies typically extend  $< 10$  kpc from the source, this is more likely caused by the faintness in the stellar continuum at larger radii rather than an intrinsic property of the outflow. The absorption in this system is not down-the-barrel, but the quasar sightline is only 18 (9) kpc from galaxy B (A). Hence, component 2, which is traced by Na I and Ca II without corresponding 21-cm absorption in the radio, is possibly wind material.

### 5.3 Inflows

Galaxies require replenishment of their gas reservoirs to sustain their star formation rates. Contrary to outflows, cold gas accreting from dark matter filaments are expected to align preferentially with the galaxy major axis in the form of an extended cold gas disc (Ho et al. 2019). For galaxy B, its azimuthal angle of  $57^\circ$  indicates the orientation is not favourable for probing an extended gaseous disc. Further, studies of accreting gas using quasar absorption line spectroscopy select a single ‘primary’ galaxy most likely associated with the absorber (e.g. Zabl et al. 2019). In our case, both galaxies A and B are located within 20 kpc and  $100 \text{ km s}^{-1}$  of the absorber and it becomes difficult to distinguish between inflows and gas structures emerging from interactions between galaxies.

### 5.4 Extragalactic Gas Clouds

H I emission maps of local interacting galaxy pairs and groups reveal extragalactic clouds of gas (e.g. Verdes-Montenegro et al. 2001; Lee-Waddell et al. 2019). This phenomena has also been possibly detected at higher redshift in a radio galaxy interacting with a satellite (Allison et al. 2019) using H I absorption and ALMA observations. These clouds are typically high column density ( $\sim 10^{20} \text{ cm}^{-2}$ ) and of similar velocity to nearby galaxies. Galaxies A and B are separated by 17 kpc with only a  $60 \text{ km s}^{-1}$  velocity difference and Figure 7 reveals they share the same velocity plane, with the redshifted side of galaxy B extending towards galaxy A. Additionally, the significant contribution of A-type stellar templates during PPXF fitting is indicative of a significant young stellar population. This suggests a period of enhanced star formation several 100 Myrs in the past, most likely induced by interactions between galaxies A and B. Extragalactic clouds resulting from this interaction are possible explanations for components 1a and 1b seen in absorption.

### 5.5 Nature of the Gas

The wealth of information obtained from the ASKAP and MUSE instruments allows us gain a greater understanding of the gas seen in absorption. Components 1a and 1b from the initial radio detection cannot be explained by the rotating disc of galaxy B, and the emission lines of nearest group member galaxy A are too low S/N to discern ionized gas velocities for comparison with the neutral gas kinematics. Instead, a more likely scenario is that the 21-cm detection probes extragalactic gas clouds formed by interactions between galaxies A and B. While outflows from galaxy B cannot be excluded, it is questionable whether such dense amounts of cold neutral gas will still be found in ejected material roughly 20 kpc from the source. Additional constraints on this scenario can be applied if the DLA metallicity is known and then compared with the galaxy metallicity. The absence of metallicity information also means there is not enough information to conclude that component 2 derived from Na I and Ca II absorption is a result of inflows. At this stage, we favour the scenario that component 2 traces gas that is part of galaxy B's disc due to its alignment in velocity with the redshifted side of the galaxy.

## 6 CONCLUSION

Through the novel and powerful combination of ASKAP and MUSE instruments, the nature of gas in this system has been successfully probed. The neutral hydrogen absorption detection with the Australian Square Kilometre Array Pathfinder telescope reveals two components (1a and 1b) near  $z = 0.4503$  separated by  $43 \text{ km s}^{-1}$  (Sadler et al. 2020). From the MUSE spectrum of QSO PKS 1610-771, strong absorption from ions Ca II and Na I are found. A component of these low-ionisation metals coincides with the neutral gas detected by ASKAP, while the other component (2) reveals another cloud of gas redshifted by  $\sim 180 \text{ km s}^{-1}$  from the first. Component 2 is likely of lower column density or higher temperature and thus, is not found in the initial radio detection. In total, three components of gas are found in front of PKS 1610-771 due to an overlap between the neutral hydrogen and low-ionisation metal components.

Imaging of the system from Courbin et al. (1997) reveals four galaxy-like objects (A, B, C and D) near PKS 1610-771. Using the MUSE datacube which has spectral information for objects in a  $1 \times 1 \text{ arcmin}^2$  field-of-view, object C is determined to be a faint M-type star. To uncover the redshift of galaxy D outshone by the bright QSO, a 1D spectral PSF subtraction is performed and reveals its redshift to likely be  $z \sim 0.5$  using corroborating evidence from Hunstead & Murdoch (1980). While objects C and D are not part of the direct group, narrowband imaging around the [O II] emission line reveals two other galaxies (X and Y) located at a projected distance of more than 100 kpc from the quasar. In total, there are four objects found at the redshift of the DLA and these align in what appears to be a filamentary structure.

Galaxies A and B are located at projected distances of 8.82 and 17.76 kpc from the absorber respectively, while X and Y are further afield (136 and 190 kpc respectively). In velocity space, galaxies X and Y are also further from the

DLA with redshifts  $z_X = 0.45279$  and  $z_Y = 0.45129$ . In contrast, galaxies A and B are separated by 93 and  $24 \text{ km s}^{-1}$  from  $z_{\text{abs}} = 0.4503$ . Curiously, three of the four galaxy spectra (A, B and Y) have higher-order Balmer lines, suggesting an enhanced period of star formation in the past several hundred Myrs caused by interactions. The SFR of galaxy B is high at  $4.3 \text{ M}_{\odot} \text{ yr}^{-1}$  after correction for dust extinction, but none of the other group members are completely passive with  $\text{SFR} > 0.2 \text{ M}_{\odot} \text{ yr}^{-1}$ . From fitting of the ionized gas kinematics, there is clear rotation in the ionized disc of galaxy B. Galaxies A, X and Y have emission lines with low S/N or are too compact to fit for kinematics.

The three components of gas in front of the quasar have velocities of  $-59$  (1a),  $-16.0$  (1b) and  $\sim 160 \text{ km s}^{-1}$  (2) with respect to the systemic velocity of galaxy B. As the redshifted side of galaxy B's ionized disc is aligned with the QSO sightline, only component 2 can be a result of co-rotation with the disc. The azimuthal angle between the projected major axis of star-forming galaxy B and the DLA is found to be  $\alpha = 57^\circ$ , which is consistent with biconical outflows. However, assuming a spin temperature of 1000 K for the outflowing H I produces unlikely column densities  $N_{\text{H I}} > 2 \times 10^{21} \text{ atoms cm}^{-2}$  for components 1a and 1b. It is possible that component 2 does trace outflowing material from galaxy B as the gas traced is likely higher temperature and lower H I column density. Galaxies A and B are only separated by  $\sim 17 \text{ kpc}$  and we conclude components 1a and 1b in front of the quasar are most likely a result of extragalactic gas clouds from this pair interacting or merging. The additional higher-velocity component seen in MUSE (2) is likely associated with the co-rotation of galaxy B's disc, although outflowing wind material cannot be excluded.

The gas traced in absorption is inevitably a combination of the scenarios mentioned above. While exact identification of the phenomena responsible for the absorption features seen in the ASKAP and MUSE spectra is uncertain, this work already illustrates the intricacies of gas behaviour at a largely unexplored redshift. With the emergence of large H I surveys such as the First Large Absorption Survey in H I (Allison et al. 2020, Allison et al, in prep.) and the MeerKAT Large Absorption Line Survey (MALS) (Gupta et al. 2016), the amount and kinematics of cold neutral gas in hundreds of systems will be determined at largely unexplored redshifts. Contained within each of these individual detections is a puzzle waiting to be unravelled: what are the origins of the neutral gas in relation to its associated galaxies? If answered within enough systems by combining with optical or millimetre observations, we are able to gain insights into the impact of gas on galaxy evolution during an era in the Universe not well understood.

## DATA AVAILABILITY

The data underlying this article will be shared on reasonable request to the corresponding author.

## ACKNOWLEDGEMENTS

We acknowledge the financial support of the Australian Research Council through grant CE170100013 (ASTRO3D).

Based on observations collected at the European Southern Observatory under ESO programme 0103.A-0656. We thank Thomas Ott for developing and distributing the QFITSVIEW software. This research made use of Astropy,<sup>5</sup> a community-developed core Python package for Astronomy (Astropy Collaboration et al. 2013, 2018). This research is supported by an Australian Government Research Training Program (RTP) Scholarship.

## REFERENCES

- Allison J. R., Sadler E. M., Whiting M. T., 2012, *Publ. Astron. Soc. Australia*, **29**, 221
- Allison J. R., et al., 2019, *MNRAS*, **482**, 2934
- Allison J. R., et al., 2020, *MNRAS*, **494**, 3627
- Astropy Collaboration et al., 2013, *A&A*, **558**, A33
- Astropy Collaboration et al., 2018, *AJ*, **156**, 123
- Bacon R., Piqueras L., Conseil S., Richard J., Shepherd M., 2016, MPDAF: MUSE Python Data Analysis Framework (ascl:1611.003)
- Bekhti N. B., Richter P., Westmeier T., Murphy M. T., 2008, *Astronomy & Astrophysics*, **487**, 583
- Berg T. A. M., et al., 2019, *MNRAS*, **488**, 4356
- Boomsma R., Oosterloo T. A., Fraternali F., van der Hulst J. M., Sancisi R., 2008, *Astronomy & Astrophysics*, **490**, 555
- Borthakur S., 2016, *ApJ*, **829**, 128
- Bouché N., Murphy M. T., Péroux C., Davies R., Eisenhauer F., Schreiber N. M. F., Tacconi L., 2007, *The Astrophysical Journal*, **669**, L5
- Bouché N., Carfanten H., Schroetter I., Michel-Dansac L., Contini T., 2015, *AJ*, **150**, 92
- Braun R., 2012, *ApJ*, **749**, 87
- Brown R. L., Mitchell K. J., 1983, *ApJ*, **264**, 87
- Cappellari M., 2017, *Monthly Notices of the Royal Astronomical Society*, **466**, 798
- Cappellari M., Emsellem E., 2004, *Publications of the Astronomical Society of the Pacific*, **116**, 138
- Carswell R. F., Webb J. K., 2014, VPFIT: Voigt profile fitting program (ascl:1408.015)
- Cazzoli S., Arribas S., Maiolino R., Colina L., 2016, *Astronomy & Astrophysics*, **590**, A125
- Chowdhury A., Kanekar N., Chengalur J. N., Sethi S., Dwarakanath K. S., 2020, *Nature*, **586**, 369
- Courbin F., Hutsemekers D., Meylan G., Magain P., Djorgovski S. G., 1997, *Astronomy & Astrophysics*, **317**, 656
- Curran S. J., Reeves S. N., Allison J. R., Sadler E. M., 2016, *MNRAS*, **459**, 4136
- Darling J., Giovanelli R., Haynes M. P., Bolatto A. D., Bower G. C., 2004, *ApJ*, **613**, L101
- DeBoer D. R., et al., 2009, *Proceedings of the IEEE*, **97**, 1507
- Dutta R., Srianand R., Gupta N., Momjian E., Noterdaeme P., Petitjean P., Rahmani H., 2017, *MNRAS*, **465**, 588
- Falcón-Barroso J., Sánchez-Blázquez P., Vazdekis A., Ricciardelli E., Cardiel N., Cenarro A. J., Gorgas J., Peletier R. F., 2011, *Astronomy & Astrophysics*, **532**, A95
- Giovanelli R., Haynes M. P., 2015, *A&ARv*, **24**, 1
- Gronke M., Oh S. P., 2018, *MNRAS*, **480**, L111
- Gronke M., Oh S. P., 2020, *MNRAS*, **492**, 1970
- Gupta N., et al., 2016, in MeerKAT Science: On the Pathway to the SKA. p. 14 (arXiv:1708.07371)
- Hamanowicz A., et al., 2020, *Monthly Notices of the Royal Astronomical Society*, **493**, 446
- Heckman T. M., Lehnert M. D., Strickland D. K., Armus L., 2000, *ApJS*, **129**, 493
- Ho S. H., Martin C. L., Turner M. L., 2019, *ApJ*, **875**, 54
- Hoppmann L., Staveley-Smith L., Freudling W., Zwaan M. A., Minchin R. F., Calabretta M. R., 2015, *Monthly Notices of the Royal Astronomical Society*, **452**, 3726
- Hotan A. W., et al., 2014, *Publ. Astron. Soc. Aust.*, **31**
- Hotan A. W., et al., 2021, *Publ. Astron. Soc. Australia*, **38**, e009
- Hunstead R. W., Murdoch H. S., 1980, *MNRAS*, **192**, 31P
- Husemann B., Bennert V. N., Scharwächter J., Woo J.-H., Choudhury O. S., 2016, *Monthly Notices of the Royal Astronomical Society*, **455**, 1905
- Johnston S., et al., 2007, *Publ. Astron. Soc. Australia*, **24**, 174
- Jonas J., MeerKAT Team 2016, in MeerKAT Science: On the Pathway to the SKA. p. 1
- Jones M. G., Haynes M. P., Giovanelli R., Moorman C., 2018, *Monthly Notices of the Royal Astronomical Society*, **477**, 2
- Kanekar N., Sethi S., Dwarakanath K. S., 2016, *ApJ*, **818**, L28
- Kennicutt R. C., 1998, *Annual Review of Astronomy and Astrophysics*, **36**, 189
- Kewley L. J., Geller M. J., Jansen R. A., 2004, *AJ*, **127**, 2002
- Klitsch A., Péroux C., Zwaan M. A., Smail I., Oteo I., Biggs A. D., Popping G., Swinbank A. M., 2017, *Monthly Notices of the Royal Astronomical Society*, **475**, 492
- Krajnović D., Cappellari M., de Zeeuw P. T., Copin Y., 2006, *MNRAS*, **366**, 787
- Krogager J.-K., Fynbo J. P. U., Møller P., Noterdaeme P., Heintz K. E., Pettini M., 2019, *MNRAS*, **486**, 4377
- Lee-Waddell K., et al., 2019, *Monthly Notices of the Royal Astronomical Society*, **487**, 5248
- McConnell D., et al., 2016, *Publ. Astron. Soc. Aust.*, **33**
- Murray C. E., Stanimirović S., Goss W. M., Heiles C., Dickey J. M., Babler B., Kim C.-G., 2018, *The Astrophysical Journal Supplement Series*, **238**, 14
- Neeleman M., Prochaska J. X., Ribaud J., Lehner N., Howk J. C., Rafelski M., Kanekar N., 2016, *ApJ*, **818**, 113
- Nelson D., et al., 2019, *Monthly Notices of the Royal Astronomical Society*, **490**, 3234
- Noterdaeme P., Petitjean P., Ledoux C., Srianand R., 2009, *A&A*, **505**, 1087
- Noterdaeme P., et al., 2012, *A&A*, **547**, L1
- Ojha R., et al., 2010, *Astronomy and Astrophysics*, **519**, A45
- Osterbrock D. E., 1989, *Astrophysics of gaseous nebulae and active galactic nuclei*
- Péroux C., Howk J. C., 2020, *ARA&A*, **58**, 363
- Péroux C., McMahon R. G., Storrie-Lombardi L. J., Irwin M. J., 2003, *MNRAS*, **346**, 1103
- Péroux C., Bouché N., Kulkarni V. P., York D. G., Vladilo G., 2011, *Monthly Notices of the Royal Astronomical Society*, **410**, 2237
- Péroux C., Bouché N., Kulkarni V. P., York D. G., 2013, *Monthly Notices of the Royal Astronomical Society*, **436**, 2650
- Péroux C., et al., 2016, *Monthly Notices of the Royal Astronomical Society*, **464**, 2053
- Péroux C., et al., 2019, *Monthly Notices of the Royal Astronomical Society*, **485**, 1595
- Péroux C., Nelson D., van de Voort F., Pillepich A., Marinacci F., Vogelsberger M., Hernquist L., 2020, *MNRAS*, **499**, 2462
- Pontzen A., Pettini M., 2009, *MNRAS*, **393**, 557
- Rahmani H., et al., 2018, *MNRAS*, **480**, 5046
- Rao S., Briggs F., 1993, *ApJ*, **419**, 515
- Rao S. M., Turnshek D. A., 2000, *The Astrophysical Journal Supplement Series*, **130**, 1
- Rao S. M., Turnshek D. A., Nestor D. B., 2006, *The Astrophysical Journal*, **636**, 610
- Rao S. M., Turnshek D. A., Sardane G. M., Monier E. M., 2017, *MNRAS*, **471**, 3428
- Reeves S. N., et al., 2016, *MNRAS*, **457**, 2613

<sup>5</sup> <http://www.astropy.org>

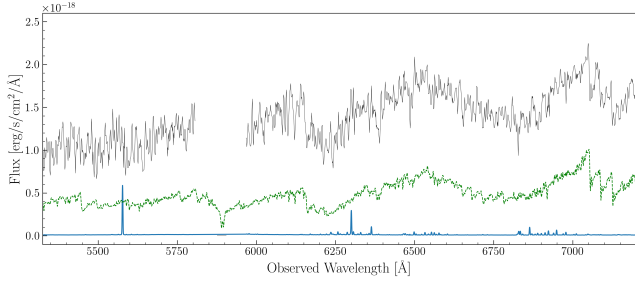


**Figure A1.** A smoothed (3 pixel moving average) spectrum of object C is plotted in black with the corresponding sky spectrum in blue (not to scale). An arbitrarily scaled spectrum of M5V type star HD 173740 is plotted in green for comparison.

- Rhee J., Lah P., Briggs F. H., Chengalur J. N., Colless M., Willner S. P., Ashby M. L. N., Le Fèvre O., 2018, *MNRAS*, **473**, 1879  
 Richter P., Westmeier T., Brüns C., 2005, *Astronomy & Astrophysics*, **442**, L49  
 Robotham A. S. G., Davies L. J. M., Driver S. P., Koushan S., Taranu D. S., Casura S., Liske J., 2018, *Monthly Notices of the Royal Astronomical Society*, **476**, 3137  
 Rosenberg J. L., Schneider S. E., 2002, *The Astrophysical Journal*, **567**, 247  
 Sadler E. M., et al., 2020, *MNRAS*, **499**, 4293  
 Sanchez-Blazquez P., et al., 2006, *Monthly Notices of the Royal Astronomical Society*, **371**, 703  
 Schroetter I., et al., 2019, *MNRAS*, **490**, 4368  
 Veilleux S., Cecil G., Bland-Hawthorn J., 2005, *Annual Review of Astronomy and Astrophysics*, **43**, 769  
 Verdes-Montenegro L., Yun M. S., Williams B. A., Huchtmeier W. K., Olmo A. D., Perea J., 2001, *Astronomy & Astrophysics*, **377**, 812  
 Weilbacher P. M., Streicher O., Urrutia T., Jarno A., Pécontal-Rousset A., Bacon R., Böhm P., 2016, in Radziwill N. M., Chiozzi G., eds, *Software and Cyberinfrastructure for Astronomy II*. SPIE, doi:10.1117/12.925114  
 Zabl J., et al., 2019, *MNRAS*, **485**, 1961  
 Zafar T., Péroux C., Popping A., Milliard B., Deharveng J. M., Frank S., 2013, *A&A*, **556**, A141  
 Zwaan M. A., Meyer M. J., Staveley-Smith L., Webster R. L., 2005, *Monthly Notices of the Royal Astronomical Society*, **359**, L30

## APPENDIX A: OBJECTS C AND D

Despite the proximity of objects C and D to the absorber on the sky, none is associated with the DLA. The former is evidently a faint M-type star from Figure A1.

After the 3D PSF subtraction to unearth object D, there are two candidate emission lines in its spectrum near 5587 and 7290 Å, and these are reproduced in Figure A2. The two emission lines are consistent with [O II] and Hβ at  $z = 0.5001$ . Thus, galaxy D is unlikely to be associated with the DLA, but may trace a larger scale structure.

## APPENDIX B: GALAXY SPECTRA

The MUSE spectra of the galaxy group members at  $z = 0.45$  are displayed in this appendix. For three of the objects (A, B and Y), the stellar continuum is clearly detected, while

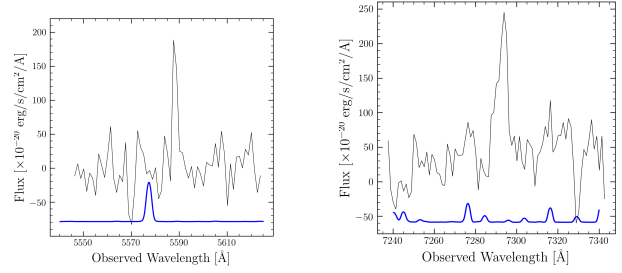


**Figure A2.** Candidate emission lines O II (left) and Hβ (right) found in front of QSO PKS 1610-771 after a 1D PSF subtraction (black). Scaled and vertically offset sky spectrum is in blue. The best-fitting redshifts is  $z = 0.5001$  for the pair of lines.

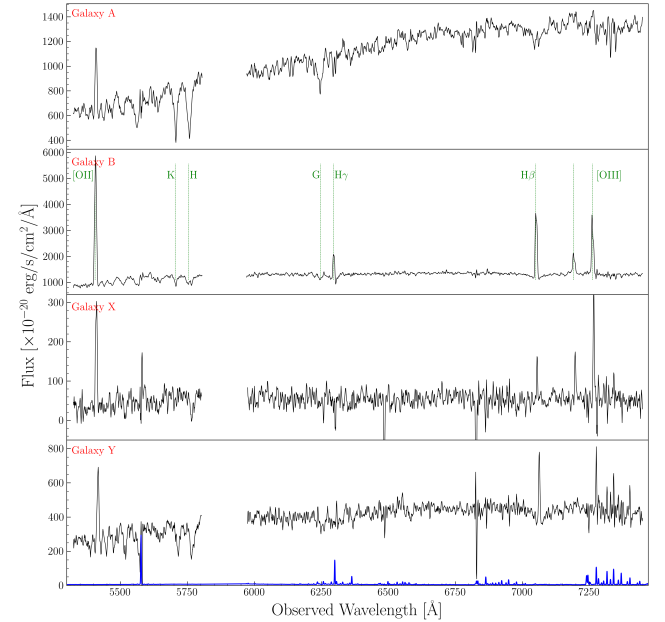


**Figure B1.** Spectra of the four galaxies associated with the  $z = 0.45$  absorber (A, B, X and Y from top to bottom) from MUSE. Emission and absorption lines are marked on the spectrum of galaxy B and can also be seen in the remaining group members. A scaled and vertically offset sky spectrum is included in blue. Each spectrum has been smoothed using a 3 pixel moving average.

emission lines are prevalent in all spectra. Poorer sky subtraction near the edges of the MUSE field result in artefacts at 6500 and 6850 Å in the spectra of galaxies X and Y. The spectral gap from 5800 Å to 6000 Å is due to the use of the AO system consisting of Na I D lasers.

## APPENDIX C: PKS 1610-771 METAL LINES

Another system at redshift  $z = 1.621$  can be seen in the the background quasar through various absorption lines (Si II, Al III, Fe II, Mn II, Mg II and Mg I). These are marked in green in Figure C1 along with the broad emission lines of the QSO (red) and Ca II and Na I absorption linked to our H I detection. However, the significant disparity in redshift means this higher redshift system is not related to our absorber.



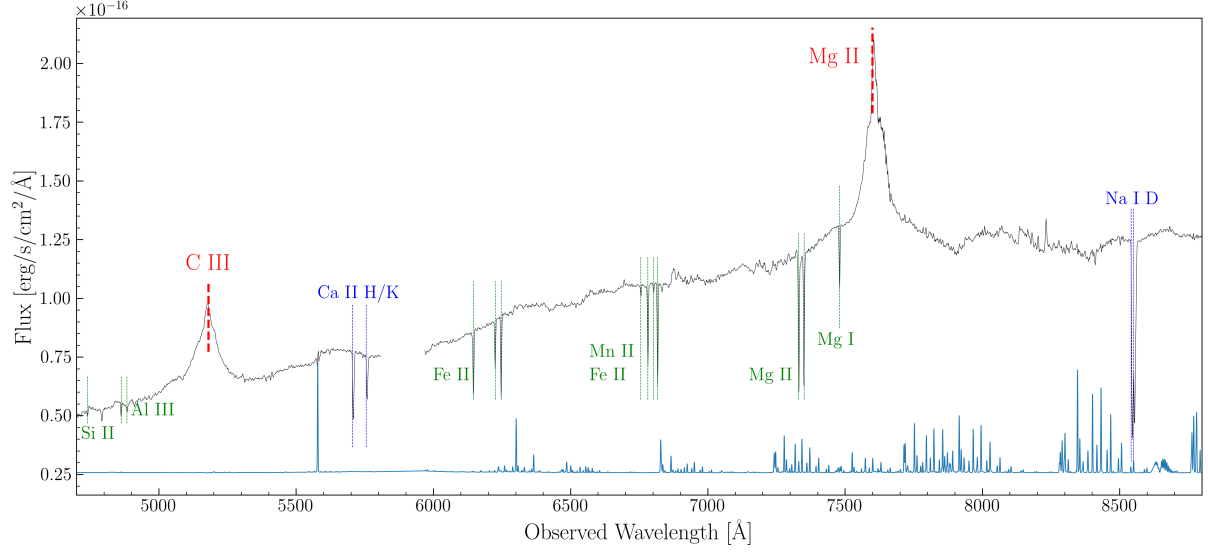


**Figure C1.** A smoothed (3 pixel moving average) spectrum of the QSO with the corresponding sky spectrum in blue (not to scale). Marked in red are the broad emission lines of the quasar (Mg II and C III) at  $z = 1.71$ . A separate metal system (green) is found at redshift  $z = 1.621$ , but this is not associated with the DLA. Instead, Ca II and Na I metal absorption lines marked in blue are at the redshift of the  $z = 0.45$  absorber.

This paper has been typeset from a  $\text{\LaTeX}$  file prepared by the author.